A High Order Semi-Lagrangian Finite Difference Method for nonlinear Vlasov and BGK Models

Linjin Li[1], Jingmei Qiu[2], Giovanni Russo[3].

Abstract. In this paper, we propose a new conservative high order semi-Lagrangian finite difference (SLFD) method to solve linear advection equation, and the nonlinear Vlasov and BGK models. The finite difference scheme has better computational flexibility by working with point values, especially when working with high dimensional problems in an operator splitting setting. The reconstruction procedure in the proposed SLFD scheme is motivated from the semi-Lagrangian finite volume scheme. In particular, we define a new sliding average function, whose cell averages agree with point values of the underlying function. By developing semi-Lagrangian finite volume scheme for the sliding average function, we derive the proposed SLFD scheme, which is high order accurate, mass conservative, and unconditionally stable for linear problems. The performance of the scheme is showcased by linear transport applications, as well as the nonlinear Vlasov-Poisson and BGK models. Further more, we apply the Fourier stability analysis to a fully discrete SLFD scheme coupled with diagonally implicit Runge-Kutta (DIRK) method when applied to a stiff two-velocity hyperbolic relaxation system. Numerical stability and asymptotic accuracy properties of DIRK methods are discussed in theoretical and computational aspects.

Key Words: Semi-Lagrangian; WENO; Finite difference; Vlasov-Poisson; BGK equation, linear stability.

1 Introduction

Kinetic models describe the dynamics of mesoscale particles by their probability distribution function. The models lie in between the microscopic particles dynamics governed by Newton's laws of motion and macroscopic fluid dynamics. A kinetic model provides a complete phase-space de-

[1]Department of Mathematical Sciences, University of Delaware, Newark, DE, 19717. E-mail: llj@udel.edu

[2]Department of Mathematical Sciences, University of Delaware, Newark, DE, 19717. E-mail: jingqiu@udel.edu. Research of first and second authors are supported by NSF grant NSF-DMS-1818924, Air Force Office of Scientific Computing FA9550-18-1-0257 and University of Delaware.

[3]Department of Mathematics and Computer Science, University of Catania, Italy, E-mail: grusso@dmi.unict.it. The third author would like to thank the Italian Ministry of Instruction, University and Research (MIUR) to support this research with funds coming from PRIN Project 2017, No. 2017KKJP4X and ITN-ETN Horizon 2020 Project, Project Reference 642768.

scription of particle distribution by introducing velocities as new independent variables. When considering the charged particles, particle dynamics are subject to external and self-induced electromagnetic fields and interparticle collisions, which lead to the Vlasov term and the collision term in kinetic models. In the kinetic model, particle dynamics in the phase spaces are characterized by transport terms, for which semi-Lagrangian methodology becomes a competitive tool, thanks to its numerical stability free of CFL type time step restriction.

The semi-Lagrangian (SL) methods have been under great development for more than three decades. It has been shown to be advantageous compared with traditional Eulerian and Lagrangian approaches, for example in climate [16, 12, 13] and kinetic [9, 20, 4, 23] models. In fact, it is designed to take advantage of the Eulerian approach by working with a fixed set of computational mesh and developing corresponding high resolution methodologies, and take advantage of the Lagrangian approach by tracking information along characteristics thus avoid the stringent CFL time step constraint. Different classes of SL methods have been developed in parallel, including the volume-based finite element, finite volume methods and point-based finite difference (FD) method. In this work, we consider the SL FD method for better flexibility in handling high dimensional problems in the operator splitting setting, and better robustness when the nonlinear WENO techniques [2, 20] are applied in the reconstruction process. However, SLFD often lost mass conservation especially when the nonlinear WENO procedure is applied [2]. In [20, 21], the authors proposed to work with the flux difference form for local mass conservation. Here in this work, we take a different approach by working with the sliding average functions, for which a mass conservative SL finite volume WENO scheme is developed. The newly developed SLFD is high order accurate, is robust for capturing solutions with sharp gradients without numerical oscillations, and is mass conservative. It is applied to the linear transport equation, the nonlinear Vlasov-Poisson (VP) and multi-scale BGK models.

Coupling the SL approach with implicit time integrators along characteristics for stiff relaxation models have been explored computationally and theoretically [24, 7]. The stiffness of the relaxation model is often characterized by a parameter ϵ. In the BGK model, ϵ stands for the Knudsen number to characterized the rarefied gas. Yet, little is done to theoretically investigate asymptotic accuracy and numerical stability of a fully discrete scheme. In fact, in [11], order reduction is computationally observed for a classical third order DIRK method, for which only a second order convergence is

observed in the asymptotic limit of ϵ goes to zero. In [7], linear stability analysis is performed for the semi-discrete DIRK methods with continuous in spatial variables for a simple 2-by-2 two-velocity model. In this work, we follow up with those work and perform a linear stability analysis for a fully discrete SLFD-DIRK scheme for a two-velocity model. Several third order linearly stable and asymptotically accurate DIRK methods are identified and applied for linear and nonlinear stiff relaxation models.

The paper is organized as follows. In Section 2, we shortly review finite volume (FV) and semi-Lagrangian finite volume (SLFV) scheme, then introduce the new SLFD scheme. The new scheme is applied to nonlinear VP and BGK models in Section 3, along with a stability analysis for a two-velocity relaxation model in BGK. Section 4 presents numerical simulation results. Finally, the conclusion is given in Section 5.

2 A new SLFD scheme

In this section, we will first briefly review FV and SLFV scheme with WENO reconstruction for solving the 1-D advection equation. Built upon the SLFV scheme, we propose a new SLFD scheme that has the property of mass conservation and high order spatial accuracy.

2.1 FV and SLFV scheme

We introduce the FV method using a 1-D linear advection equation as an example:

$$u_t + (cu)_x = 0, \text{ on } [a, b], \tag{2.1}$$

with the initial condition $u(x, t = 0) = u_0(x)$. We assume periodic boundary condition. For domain discretization, we use uniform cells $I_i = [x_{i-\frac{1}{2}}, x_{i+\frac{1}{2}}]$ where $i = 1, 2, ..., N$ and $\Delta x = x_{i+\frac{1}{2}} - x_{i-\frac{1}{2}}$. The FV formulation is derived from the integral form of equation (2.1) on each cell I_i:

$$\frac{d}{dt}\bar{u}_i(t) = -\frac{1}{\Delta x}\left(\hat{f}_{i+\frac{1}{2}} - \hat{f}_{i-\frac{1}{2}}\right). \tag{2.2}$$

Here $\bar{u}_i = \frac{1}{\Delta x}\int_{I_i} u(\xi, t)d\xi$ denotes the cell average of the solution, and $\hat{f}_{i+\frac{1}{2}} = \hat{f}(u^-_{i+\frac{1}{2}}, u^+_{i+\frac{1}{2}})$ is the numerical flux. The values of $u^{\pm}_{i+\frac{1}{2}}$ can be reconstructed in a WENO fashion from the cell averages in a neighborhood stencil $(u_{i-p}, ..., u_{i+q})$. Specifically, one more point from the left will be taken to reconstruct $u^-_{i+\frac{1}{2}}$, and one more point from the right will be taken to reconstruct $u^+_{i+\frac{1}{2}}$. For example, for a third order WENO scheme, we use the 3-cell stencil $S_1 = \{I_{i-1}, I_i, I_{i+1}\}$ to

reconstruct $u^-_{i+\frac{1}{2}}$, and $S_2 = \{I_i, I_{i+1}, I_{i+2}\}$ to reconstruct $u^+_{i+\frac{1}{2}}$. More specifically, to reconstruct $u^-_{i+\frac{1}{2}}$, we reconstruct a polynomial $p_1(x)$ on I_i such that its cell average agree with the cell average of $u(x)$ over the stencil S_1, in the sense that

$$\bar{u}_j = \frac{1}{\Delta x}\int_{x_{j-\frac{1}{2}}}^{x_{j+\frac{1}{2}}} p_1(x)\ dx,\ j \in S_1. \tag{2.3}$$

One could then use $p_1(x_{i+\frac{1}{2}})$ as an approximation to the value $u^-_{i+\frac{1}{2}}$. Similarly for approximating $u^+_{i+\frac{1}{2}}$. For more details, we refer to [17, 25]. The flux is designed respecting the upwind principle, i.e. $\hat{f}_{i\pm\frac{1}{2}}$ is Lipschitz continuous and monotonically increasing/decreasing with respect to first/second argument. With the above described spatial discretization, (2.2) becomes a system of time dependent ODEs, for which strong stability preserving (SSP) Runge-Kutta (RK) [10] methods can be applied via the method of lines (MOL) approach. Such method belongs to the class of Eulerian approach, in which the CFL is a well-known stability restriction on time stepping size.

On the other hand, in a SL scheme, characteristic tracking is a critical step to avoid CFL time step restriction. From cell boundaries, there exist backward characteristic lines with their feet located on time level t^n. Since there is no flux passing through the characteristic lines, due to mass conservation, the cell averages for equation (2.1) can be updated in the following way, see Fig. 2.1:

$$\begin{aligned}\bar{u}_i^{n+1} &= \frac{1}{\Delta x}\int_{x_{i-\frac{1}{2}}}^{x_{i+\frac{1}{2}}} u(x,t^{n+1})dx = \frac{1}{\Delta x}\int_{y_{i-\frac{1}{2}}}^{y_{i+\frac{1}{2}}} u(x,t^n)\ dx \\ &= \frac{1}{\Delta x}\int_{y_{i-\frac{1}{2}}}^{x_{i-\frac{1}{2}}} u(x,t^n)dx + \frac{1}{\Delta x}\int_{x_{i-\frac{1}{2}}}^{y_{i+\frac{1}{2}}} u(x,t^n)\ dx,\end{aligned} \tag{2.4}$$

where $y_{i\pm\frac{1}{2}} = x_{i\pm\frac{1}{2}} - c\Delta t$ are the feet of characteristics at t^n originate from $(x_{i\pm\frac{1}{2}}, t^{n+1})$. Here we consider the special case of $c > 0$ and $CFL < 1$. For more general cases with large time stepping sizes, one has to locate the feet of characteristics in the computational mesh in order to identify subintervals for integration in equation (2.4).

To update $\bar{u}_i^{n+1}$, the first step is to approximate $u(x,t^n)$ by polynomials on each computational cell using the classical WENO reconstruction [26, 25]. We construct $p(x)$ as the polynomial of degree 4 on cell I_i from a 5-point stencil $S = \{I_{i-2}, I_{i-1}, I_i, I_{i+1}, I_{i+2}\}$ in a similar manner as in equation (2.3). Stencil S can be decomposed into three 3-point stencils $S_1 = \{I_{i-2}, I_{i-1}, I_i\}$, $S_2 = \{I_{i-1}, I_i, I_{i+1}\}$, $S_3 = \{I_i, I_{i+1}, I_{i+2}\}$. We can also find polynomials $p_k(x)$ of degree 2 reconstructing the cell averages of function $u(x)$ on each stencil S_k for $k = 1, 2, 3$ by the same process. Let $\xi = \frac{x-x_i}{\Delta x}$

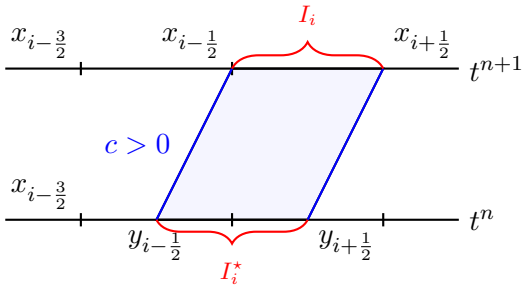

Figure 2.1: SLFV formulation for equation (2.1)

be a mapping from I_i to a reference interval $[-\frac{1}{2}, \frac{1}{2}]$. The explicit formulas are:

$$
\begin{aligned}
p_1(\xi) &= \frac{1}{2}\big(\bar{u}_i - 2\bar{u}_{i-1} + \bar{u}_{i-2}\big)\xi^2 + \frac{1}{2}\big(3\bar{u}_i - 4\bar{u}_{i-1} + \bar{u}_{i-2}\big)\xi + \frac{1}{24}\big(23\bar{u}_i + 2\bar{u}_{i-1} - \bar{u}_{i-2}\big),\\
p_2(\xi) &= \big(\frac{1}{2}\bar{u}_{i-1} + \frac{1}{2}\bar{u}_{i+1} - \bar{u}_i\big)\xi^2 + \frac{1}{2}\big(\bar{u}_{i+1} - \bar{u}_{i-1}\big)\xi + \big(\frac{13}{12}\bar{u}_i - \frac{1}{24}\bar{u}_{i+1} - \frac{1}{24}\bar{u}_{i-1}\big),\\
p_3(\xi) &= \frac{1}{2}\big(\bar{u}_i - 2\bar{u}_{i+1} + \bar{u}_{i+2}\big)\xi^2 + \frac{1}{2}\big(-3\bar{u}_i + 4\bar{u}_{i-1} - \bar{u}_{i-2}\big)\xi + \frac{1}{24}\big(23\bar{u}_i + 2\bar{u}_{i+1} - \bar{u}_{i+2}\big),
\end{aligned}
$$

and

$$
\begin{aligned}
p(\xi) = &\frac{1}{24}\big(6\bar{u}_i - 4\bar{u}_{i+1} + \bar{u}_{i+2} - 4\bar{u}_{i-1} + \bar{u}_{i-2}\big)\xi^4 + \frac{1}{12}\big(-2\bar{u}_{i+1} + \bar{u}_{i+2} + 2\bar{u}_{i-1} - \bar{u}_{i-2}\big)\xi^3\\
&+ \frac{1}{16}\big(-22\bar{u}_i + 12\bar{u}_{i+1} - \bar{u}_{i+2} + 12\bar{u}_{i-1} - \bar{u}_{i-2}\big)\xi^2 + \frac{1}{48}\big(34\bar{u}_{i+1} - 5\bar{u}_{i+2} - 34\bar{u}_{i-1} + 5\bar{u}_{i-2}\big)\xi\\
&+ \frac{1}{1920}\big(2134\bar{u}_i - 116\bar{u}_{i+1} + 9\bar{u}_{i+2} - 116\bar{u}_{i-1} + 9\bar{u}_{i-2}\big).
\end{aligned}
$$

The second step is to evaluate the integrals of $p(\xi)$ and $p_k(\xi)$. By taking integrals of $p(\xi)$ and $p_k(\xi)$, we obtain one polynomial Q of degree 5 and three polynomials Q_k for $k = 1, 2, 3$ of degree 3. For instance, for the interval of $[-\frac{1}{2}, \alpha]$, we have

$$
\begin{aligned}
Q(\alpha) &= \frac{1}{\Delta x}\int_{x_{i-\frac{1}{2}}}^{y_{i+\frac{1}{2}}} p(x)dx = \int_{-\frac{1}{2}}^{\alpha} p(\xi)\, d\xi,\\
Q_k(\alpha) &= \frac{1}{\Delta x}\int_{x_{i-\frac{1}{2}}}^{y_{i+\frac{1}{2}}} p_k(x)dx = \int_{-\frac{1}{2}}^{\alpha} p_k(\xi)\, d\xi,\ k = 1, 2, 3
\end{aligned}
$$

with $\alpha = \frac{1}{2} - CFL$. It is proved [18] that there exists 3 linear weights c_k, which are polynomials of degree 2, such that

$$
Q(\alpha) = \sum_{k=1}^{3} c_k(\alpha) Q_k(\alpha).
$$

In the fifth order case of our implementation, we have

$$
Q_1(\alpha) = \bar{u}_{i-2}\big(\frac{\alpha^3}{6} + \frac{3\alpha^2}{4} + \frac{23\alpha}{24} + \frac{5}{16}\big) + \bar{u}_{i-1}\big(-\frac{\alpha^3}{3} - \alpha^2 + \frac{\alpha}{12} + \frac{1}{4}\big) + \bar{u}_i\big(\frac{\alpha^3}{6} + \frac{\alpha^2}{4} - \frac{\alpha}{24} - \frac{1}{16}\big),
$$

$$Q_2(\alpha) = \bar{u}_{i-1}\big(\frac{\alpha^3}{6} - \frac{\alpha^2}{4} - \frac{\alpha}{24} + \frac{1}{16}\big) + \bar{u}_i\big(-\frac{\alpha^3}{3} + \frac{13\alpha}{12} + \frac{1}{2}\big) + \bar{u}_{i+1}\big(\frac{\alpha^3}{6} + \frac{\alpha^2}{4} - \frac{\alpha}{24} - \frac{1}{16}\big),$$
$$Q_3(\alpha) = \bar{u}_i\big(\frac{\alpha^3}{6} - \frac{3\alpha^2}{4} + \frac{23\alpha}{24} + \frac{11}{16}\big) + \bar{u}_{i+1}\big(-\frac{\alpha^3}{3} + \alpha^2 + \frac{\alpha}{12} - \frac{1}{4}\big) - \bar{u}_{i+2}\big(\frac{\alpha^3}{6} - \frac{\alpha^2}{4} - \frac{\alpha}{24} + \frac{1}{16}\big),$$

and

$$\begin{aligned} Q(\alpha) = {} & \bar{u}_{i-2}\big(\frac{\alpha^5}{120} - \frac{\alpha^4}{48} - \frac{\alpha^3}{48} + \frac{5\alpha^2}{96} + \frac{3\alpha}{640} - \frac{3}{256}\big) + \bar{u}_{i-1}\big(-\frac{\alpha^5}{30} + \frac{\alpha^4}{24} + \frac{\alpha^3}{4} - \frac{17\alpha^2}{48} - \frac{29\alpha}{480} + \frac{11}{128}\big) \\ & + \bar{u}_i\big(\frac{\alpha^5}{20} - \frac{11\alpha^3}{24} + \frac{1067\alpha}{960} + \frac{1}{2}\big) + \bar{u}_{i+1}\big(-\frac{\alpha^5}{30} - \frac{\alpha^4}{24} + \frac{\alpha^3}{4} + \frac{17\alpha^2}{48} - \frac{29\alpha}{480} - \frac{11}{128}\big) \\ & + \bar{u}_{i+2}\big(\frac{\alpha^5}{120} + \frac{\alpha^4}{48} - \frac{\alpha^3}{48} - \frac{5\alpha^2}{96} + \frac{3\alpha}{640} + \frac{3}{256}\big), \end{aligned}$$

with three linear weights

$$c_1(\alpha) = \frac{\alpha^2}{20} - \frac{\alpha}{5} + \frac{3}{16},\ c_2(\alpha) = \frac{5}{8} - \frac{\alpha^2}{10},\ c_3(\alpha) = \frac{\alpha^2}{20} + \frac{\alpha}{5} + \frac{3}{16}.$$

The third step is to bring in the WENO idea by choosing the nonlinear weights w_k according to the smoothness indicator β_k, which measures the relative smoothness of the function $\bar{u}(x)$ reconstructed from the stencil. The smoothness indicator is defined below:

$$\beta_k = \sum_{l=1}^{2} \Delta x^{2l-1} \int_{x_{i-\frac{1}{2}}}^{x_{i+\frac{1}{2}}} \big(\frac{d^l}{dx^l} p_k(x)\big)^2 dx.$$

Explicit formulas of β_k are:

$$\begin{aligned} \beta_1 &= \frac{12}{13}\big(\bar{u}_{i-2} - 2\bar{u}_{i-1} + \bar{u}_i\big)^2 + \frac{1}{4}\big(\bar{u}_{i-2} - 4\bar{u}_{i-1} + 3\bar{u}_i\big)^2, \\ \beta_2 &= \frac{12}{13}\big(\bar{u}_{i-1} - 2\bar{u}_i + \bar{u}_{i+1}\big)^2 + \frac{1}{4}\big(\bar{u}_{i-1} - 4\bar{u}_{i+1}\big)^2, \\ \beta_3 &= \frac{12}{13}\big(\bar{u}_i - 2\bar{u}_{i+1} + \bar{u}_{i+2}\big)^2 + \frac{1}{4}\big(3\bar{u}_i - 4\bar{u}_{i+1} + \bar{u}_{i+2}\big)^2. \end{aligned}$$

Equipped with these smoothness indicators, we can now define the nonlinear weights as

$$w_k = \frac{\tilde{w}_k}{\sum_{k=1}^{3} \tilde{w}_k}, \text{ with } \tilde{w}_k = \frac{c_k}{(\epsilon + \beta_k)^2},$$

where ϵ is chosen to be 10^{-6} to avoid division by zero.

Then, with the nonlinear weights w_k, we define $\tilde{Q}_i$ as

$$\tilde{Q}_i = \sum_{k=1}^{3} w_k Q_k. \tag{2.5}$$

Finally, from equation (2.4), we can update the cell averages by

$$\bar{u}_i^{n+1} = \bar{u}_{i-1}^n - \frac{1}{\Delta x}\left(\int_{x_{i-\frac{3}{2}}}^{y_{i-\frac{1}{2}}} p_{i-1}(x)\ dx - \int_{x_{i-\frac{1}{2}}}^{y_{i+\frac{1}{2}}} p_i(x) dx\right) = \bar{u}_{i-1}^n - \tilde{Q}_{i-1} + \tilde{Q}_i. \tag{2.6}$$

2.2 A new SLFD method

In this subsection, we present the newly proposed SLFD scheme. Previously, there have been four different formulations of conservative SLFD-WENO schemes in the literature, e.g. the ones based on flux-difference forms [21, 20] and a direct WENO one that does not have mass conservation [2]. In this paper, we introduce another formulation of mass conservative SLFD-WENO scheme, inspired by the sliding average function and the previously introduced SLFV scheme. A SLFD scheme updates point values of the solution, which has lower computational cost when extended to high dimensional setting by operator splitting algorithms.

The SLFD scheme for equation (2.1) is often developed by the fact that solution point values stay constant along characteristics $u(x_i, t^{n+1}) = u(x_i - c\Delta t, t^n)$. However, if one performs nonlinear WENO interpolation to find $u(x_i - c\Delta t, t^n)$, mass conservation will be lost [2]. In order to preserve mass conservation, we define a sliding average function $h(x,t)$, such that

$$\frac{1}{\Delta x}\int_{x-\frac{\Delta x}{2}}^{x+\frac{\Delta x}{2}} h(\xi,t)\ d\xi = u(x,t). \tag{2.7}$$

From equation (2.7), we know that

$$u(x_i,t^{n+1}) = \frac{1}{\Delta x}\int_{x_{i-\frac{1}{2}}}^{x_{i+\frac{1}{2}}} h(\xi,t^{n+1})\ d\xi,\ u(x_i - c\Delta t, t^n) = \frac{1}{\Delta x}\int_{x_{i-\frac{1}{2}}-c\Delta t}^{x_{i+\frac{1}{2}}-c\Delta t} h(\xi,t^n)\ d\xi.$$

Since $u(x_i,t^{n+1}) = u(x_i - c\Delta t, t^n)$, we obtain

$$\frac{1}{\Delta x}\int_{x_{i-\frac{1}{2}}}^{x_{i+\frac{1}{2}}} h(\xi,t^{n+1})\ d\xi = \frac{1}{\Delta x}\int_{x_{i-\frac{1}{2}}-c\Delta t}^{x_{i+\frac{1}{2}}-c\Delta t} h(\xi,t^n)\ d\xi.$$

Therefore, in order to update the point values of u, e.g. u_i^{n+1} from $u(x_i - c\Delta t, t^n)$, it is equivalent to update cell averages of h, e.g. $\frac{1}{\Delta x}\int_{x_{i-\frac{1}{2}}}^{x_{i+\frac{1}{2}}} h(\xi,t^{n+1})\ d\xi$ from the integral $\frac{1}{\Delta x}\int_{x_{i-\frac{1}{2}}-c\Delta t}^{x_{i+\frac{1}{2}}-c\Delta t} h(\xi,t^n)\ d\xi$, which can be reconstructed from the cell averages of h

$$\bar{h}_i^n = \frac{1}{\Delta x}\int_{x_{i-\frac{1}{2}}}^{x_{i+\frac{1}{2}}} h(\xi,t^n)\ d\xi = u_i^n \tag{2.8}$$

in the same way as the WENO reconstruction in the SLFV-WENO scheme described in the previous subsection. We provide a flow chart of the proposed SLFD algorithm:

Step1: Let the h function be the sliding average function of u in the following sense

$$u_i^n = \frac{1}{\Delta x}\int_{x_{i-\frac{1}{2}}}^{x_{i+\frac{1}{2}}} h(\xi,t^n)\ d\xi.$$

Step2: Update the solutions u_i^{n+1}

$$u_i^{n+1} = \Delta x u_{i-1}^n - \tilde{Q}_{i-1} + \tilde{Q}_i, \tag{2.9}$$

where $\tilde{Q}_i$ can be reconstructed in the WENO fashion to approximate the integral of h function, i.e. $\frac{1}{\Delta x}\int_{x_{i-\frac{1}{2}}}^{y_{i+\frac{1}{2}}} h(\xi, t^n)\, d\xi$ from $\bar{h}_i^n$.

It is easy to check the conservation property of our scheme. From equation (2.8), we have

$$\Delta x \sum_{i=1}^{N} u_i^{n+1} = \Delta x \sum_{i=1}^{N} \bar{h}_i^{n+1} = \sum_{i=1}^{N} \int_{x_{i-\frac{1}{2}}-c\Delta t}^{x_{i+\frac{1}{2}}-c\Delta t} h(\xi, t^n)\, d\xi = \Delta x \sum_{i=1}^{N} \bar{h}_i^n = \Delta x \sum_{i=1}^{N} u_i^n,$$

if periodic or compact boundary conditions are assumed.

Remark 2.1. Although our new SLFD works very well for advection equation with constant coefficient, it cannot be generalized to equations with variable coefficients easily. The proposed SLFD method can be extended to high dimensional and stiff relaxation problems with the help of operator splitting, such as the second order Strang splitting. The splitting schemes will be specified in details for the nonlinear Vlasov and BGK models in the next section.

3 SLFD for nonlinear kinetic Vlasov and BGK models

In this section, we will apply the proposed SLFD-WENO scheme to two kinetic models, the VP system and the BGK model, the latter of which is a simplified model for the Boltzmann equation.

3.1 The Vlasov equation for plasma physics

The Vlasov equation was first suggested for the description of plasma by Anatoly Vlasov in 1938. It is a differential equation describing time evolution of the distribution function of charged particles with long-range interaction,

$$f_t + v \cdot \nabla_x f + E(x,t) \cdot \nabla_v f = 0, \tag{3.1}$$

$$E(x,t) = -\nabla_x \phi(t,x),\ -\Delta_x \phi(t,x) = \rho(x,t), \tag{3.2}$$

where $f(x,v,t)$ describes the probability of finding a particle in phase space (x,v) at time $t > 0$, and x, v are the position and the velocity. E here is the self-consistent electrostatic field from the electrostatic potential ϕ, and $\rho(x,t) = \int_{R^3} f(x,v,t)dv - 1$ is the electron charge density with a constant ion background. Here all physical constants in (3.1) and (3.2) have been normalized to

one. Below we briefly recall some classical preservation results in the VP system. We will assess our numerical solutions by tracking these conserved quantities.

1. Preservation of the L^p norm, for $1 \leq p < \infty$.

$$\frac{d}{dt}\int_v\int_x f(x,v,t)^p \; dxdv = 0.$$

2. Preservation of the entropy

$$\frac{d}{dt}\int_v\int_x f(x,v,t)log(f(x,v,t)) \; dxdv = 0.$$

3. Preservation of the energy

$$\frac{d}{dt}(\int_v\int_x f(x,v,t)v^2 \; dxdv + \int_x E^2(x,t) \; dx) = 0.$$

In order to solve the VP system using the proposed SLFD method, we perform Strang splitting on (3.1). The Strang splitting SL method for the VP system was originally proposed in [3], and soon gained wide popularity[5, 8, 27]. The Strang Splitting reduces the high dimensional nonlinear Vlasov equation into one-dimensional advection equations, on which the high order SLFD-WENO schemes can be applied. We consider the 1D1V Vlasov equation (3.1) with $(x, v) \in \mathbb{R} \times \mathbb{R}$. The extension to higher dimensions is straightforward, yet computationally expensive. The time splitting form of equation (3.1) is,

$$\frac{\partial f}{\partial t} + v\frac{\partial f}{\partial t} = 0, \tag{3.3}$$

$$\frac{\partial f}{\partial t} + E(x,t)\frac{\partial f}{\partial v} = 0. \tag{3.4}$$

We first solve equation (3.3) for a half time step, followed by solving equation (3.4) for a full time step, followed by solving equation (3.3) for another half time step. In the dimensional splitting setting, (3.3) and (3.4) are both linear hyperbolic equations with constant velocity, which allows for a direct application of the proposed SLFD-WENO scheme. Next, we provide a flow chart for updating VP solutions $f^{n+1}(x, v)$ from $f^n(x, v)$.

Step1: Advance a half time step for equation (3.3) by the SL method

$$f^*(x,v) = \mathcal{SL}[(3.3)](f^n, \frac{1}{2}\Delta t).$$

Step2: Compute the electric field at the half step by substituting f^* into equation (3.2) and solve for $E(x, t)$. Here we apply fast Fourier transform (FFT) to solve the 1-D Poisson equation.

Step3: Advance a full time step for (3.4) by the SL method,

$$f^{**}(x,v) = \mathcal{SL}[(3.4)](f^*, \Delta t).$$

Step4: Advance a half time step for (3.3) by the SL method,

$$f^{n+1}(x,v) = \mathcal{SL}[(3.3)](f^{**}, \frac{1}{2}\Delta t).$$

3.2 The BGK model

The BGK model is a simplified model of the Boltzmann equation, which is a kinetic description of rarefied gas dynamics. It has a much simpler form of collision operator, yet qualitatively preserves the correct macroscopic moments near the fluid regime. SL methods for BGK models have recently been proposed in [22, 23, 1] with SLFD and [6] with SLDG. In [1], the author introduced a correction step for mass conservation, yet this correction step introduces a new stability restriction on time stepping sizes. Below, we will first applied the mass conservative SLFD scheme that we newly proposed to the nonlinear BGK model in Section 3.2.1. Then we will investigate numerical stability of fully discrete schemes when the SLFD scheme is coupled with DIRK schemes along characteristics in handling stiff relaxation terms in Section 3.2.2. In this context, we will consider a simplified two-velocity model, where linear Fourier analysis is allowed.

In the BGK model, the collision operator is substituted by a relaxation operator,

$$\begin{cases} \frac{df}{dt} + v \cdot \nabla_x f = \frac{1}{\epsilon}\big(M[f] - f\big) \\ f(x,v,0) = f_0(x,v), \end{cases} \tag{3.5}$$

where $(x,v,t) \in \mathbb{R}^d \times \mathbb{R}^d \times \mathbb{R}^+$, d denotes the dimension of the physical and velocity spaces. ϵ is the Knudsen number, defined as the ratio between the molecular mean free path length and a representative macroscopic length. The Knudsen number varies in a wide range, from order one in the rarefied regime to very small value in the fluid regime. $M[f]$ denotes the local Maxwellian that shares the same macroscopic moments of the distribution function $f(x,v,t)$, and is given by

$$M[f](x,v,t) = \frac{\rho(x,t)}{[2\pi RT(x,t)]^{d/2}} exp\big(-\frac{(v-u(x,t))^2}{2RT(x,t)}\big),$$

where R is the ideal gas constant and $\rho(x,t)$, $u(x,t)$ and $T(x,t)$ are the macroscopic moments of the distribution function f, that is: density, mean velocity and temperature, respectively. They are obtained in the following way:

$$\big(\rho, \rho u, E\big)^T = \int_{R^d} \phi f(v)\ dv. \tag{3.6}$$

with $\phi = (1, v, \frac{1}{2}|v|^2)^T$. The physical quantity $E(x,t)$ is the total energy which related to $T(x,t)$ through $E(x,t) = \frac{1}{2}\rho(x,t)u(x,t)^2 + \frac{d}{2}\rho(x,t)RT(x,t)$. It is easy to check that

$$\int_{R^d} M[f]\phi \, dv = (\rho, \rho u, E)^T. \tag{3.7}$$

Hence, by (3.6) and (3.7), we have

$$\int_{R^d} (M[f] - f(v))\phi \, dv = 0,$$

namely the BGK collision operator conserves the mass, momentum and energy.

We propose to apply the SLFD scheme to the convection part and treat the stiff relaxation term implicitly along characteristics. In particular, we will apply the proposed SLFD scheme coupled with the DIRK method [28, 7] for integrating the collision operator on the BGK model. Below, we will first introduce the time discretization by DIRK along characteristics; then we will treat the transport part with the proposed SLFD-WENO method. Finally, we will give a flow chart of the algorithm.

3.2.1 The SLFD-DIRK algorithm

To describe the proposed algorithm, we restrict to the 1D BGK equation. Discretizing the BGK model by considering the time evolution of $f(x,v,t)$ *along characteristic lines*, we have

$$\frac{df}{dt}(x,v,t) = \partial_t f + v \cdot \nabla_x f = \frac{1}{\epsilon}\big(M[f] - f\big). \tag{3.8}$$

Assume an s-stage DIRK method with the following Butcher table

$$\begin{array}{c|c} c & A \\ \hline & b^T \end{array}$$

where $A = (a_{i,j}) \in R^{s\times s}$ is invertible, $c = [c_1, \cdots, c_s]^T$ are the intermediate stages, and quadrature weights $b^T = [b_1, \cdots, b_s]$. Let $\Delta t = t^{n+1} - t^n$ represents a time step, and apply a DIRK method to (3.8) with the above Butcher table, we get the following scheme:

$$f^{(k)}(x,v) = f^n(x - c_k v\Delta t, v) + \frac{\Delta t}{\epsilon}\sum_{l=1}^{k} a_{kl}(M^{(l)} - f^{(l)})(x - (c_k - c_l)v\Delta t, v), \tag{3.9}$$

with $k = 1, \cdots, s$. We choose to work with stiffly accurate DIRK scheme, for which we have $f^{n+1} = f^{(s)}$.

Next, we assume uniform grid in physical and velocity space, with mesh spacing Δx and Δv respectively, and denote the grid points by $x_i, i = 0, \cdots, N_x$ and $v_j, j = 0, \cdots, N_v$. Let f_{ij}^n be the

numerical approximation to point values of $f(x_i, v_j, t^n)$. To describe the fully discrete scheme, we first consider a first order backward Euler method.

$$f_{ij}^{n+1} = \tilde{f_{ij}^n} + \frac{\Delta t}{\epsilon}\big(M[f]_{ij}^{n+1} - f_{ij}^{n+1}\big). \tag{3.10}$$

The quantity $\tilde{f_{ij}^n} = f(x_i - v_j\Delta t, v_j, t^n)$ can be computed by the proposed SLFD-WENO scheme. $M[f]_{ij}^{n+1}$ is the Maxwellian constructed with the macroscopic moments of f_{ij}^{n+1} :

$$M[f]_{ij}^{n+1} = \frac{\rho_i^{n+1}}{\sqrt{2\pi R T_i^{n+1}}} exp\big(-\frac{(v_j - u_i^{n+1})^2}{2RT_i^{n+1}}\big),$$

where discrete moments of f_{ij}^{n+1} are obtained by,

$$\rho_i^{n+1} = \sum_{j=0}^{N_v} f_{ij}^{n+1}\Delta v, \tag{3.11}$$

$$u_i^{n+1} = \frac{1}{\rho_i^{n+1}}\sum_{j=0}^{N_v} v_j f_{ij}^{n+1}\Delta v, \tag{3.12}$$

$$E_i^{n+1} = \sum_{j=0}^{N_v} \frac{1}{2} v_j^2 f_{ij}^{n+1}\Delta v. \tag{3.13}$$

From now on, we denote formulas (3.11)-(3.13) with a more compact notation $(\rho_i^{n+1}, u_i^{n+1}, E_i^{n+1}) = m[f_i^{n+1}]$, where $m[f]$ indicates the approximated macroscopic moments related to the distribution function f. To obtain $M[f_{ij}^{n+1}]$ in an explicit manner, we follow the same strategy as in [11] by taking the moments of equation (3.10); this is obtained at the discrete level multiplying both sides by $\phi_j\Delta v$, where $\phi_j = \{1, v_j, v_j^2\}$ and summing over j. Then we have $\sum_j f_{ij}^{n+1}\phi_j = \sum_j \tilde{f_{ij}^n}\phi_j$ due to the conservation property of the collision operator. Thus $m[f_i^{n+1}] \simeq m[\tilde{f_i^n}]$. Once the Maxwellian at time t^{n+1} is known using the approximated macroscopic moments $m[\tilde{f_i^n}]$, the distribution function f_{ij}^{n+1} can be explicitly computed by

$$f_{ij}^{n+1} = \frac{\epsilon\tilde{f_{ij}^n} + \Delta t M_{ij}^{n+1}}{\epsilon + \Delta t}. \tag{3.14}$$

Similar strategy could be generalized to high order time discretizations, for which we will provide a flow chart for the coupling of the SLFD-WENO method with a 3-stage DIRK time discretization on the BGK model as an example.

Step1: Compute $\tilde{f}_{ij}^{(1)} = f^n(x_i - c_1\Delta t v_j, v_j)$ at time t^n by the SLFD-WENO method. The Maxwellian $M_{ij}^{(1)}$ can be evaluated by the macroscopic moments $m[\tilde{f}_{ij}^{(1)}]$, then one can update $f_{ij}^{(1)}$

in a similar way as in (3.14) by:

$$f_{ij}^{(1)} = \frac{\epsilon \tilde{f}_{ij}^{(1)} + a_{11}\Delta t M_{ij}^{(1)}}{\epsilon + a_{11}\Delta t}.$$

Step2: Compute $\tilde{f}_{ij}^{(2)} = f^n(x_i - c_2\Delta t v_j, v_j)$ at time t^n by the SLFD-WENO method. Next compute in the same fashion $\tilde{K}_{ij}^{(2,1)}$ at $\tilde{x}^{(3)} = x_i - (c_2 - c_1)\Delta t v_j$ from $K_{ij}^{(2,1)} = \frac{1}{\epsilon}(M_{ij}^{(1)} - f_{ij}^{(1)})$ by the SLFD-WENO method. Evaluate the Maxwellian $M_{ij}^{(2)}$ using $m[\tilde{f}_{ij}^{(2)} + a_{21}\Delta t \tilde{K}_{ij}^{(2,1)}]$, then update $f_{ij}^{(2)}$ by:

$$f_{ij}^{(2)} = \tilde{f}_{ij}^{(2)} + \Delta t\big(a_{21}K_{ij}^{(2,1)} + a_{22}\frac{1}{\epsilon}(M_{ij}^{(2)} - f_{ij}^{(2)})\big),$$

the manipulation of which gives

$$f_{ij}^{(2)} = \frac{\epsilon\big(\tilde{f}_{ij}^{(2)} + a_{21}\Delta t K_{ij}^{(2,1)}\big) + a_{22}\Delta t M_{ij}^{(2)}}{\epsilon + a_{22}\Delta t}.$$

Step3: Compute $\tilde{f}_{ij}^{(3)} = f^n(x_i - c_3\Delta t v_j, v_j)$ at time t^n by the SLFD-WENO method. Then compute $\tilde{K}_{ij}^{(3,1)}$ at $\tilde{x}^{(5)} = x_i - (1 - c_1)\Delta t v_j$ and $\tilde{K}_{ij}^{(3,2)}$ at $\tilde{x}^{(6)} = x_i - (1 - c_2)\Delta t v_j$ from $\{K_{ij}^{(3,l)}\}_{i,j}$ with $K_{ij}^{(3,l)} = \frac{1}{\epsilon}(M_{ij}^{(l)} - f_{ij}^{(l)})$, $l = 1, 2$ by the SLFD-WENO method. And Maxwellian $M_{ij}^{(3)}$ can be evaluated by $m[\tilde{f}_{ij}^{(3)} + a_{31}\Delta t\tilde{K}_{ij}^{(3,1)} + a_{32}\Delta t\tilde{K}_{ij}^{(3,2)}]$. Finally we can update $f_{ij}^{(n+1)}$ by:

$$f_{ij}^{(n+1)} = \frac{\epsilon(\tilde{f}_{ij}^{(3)} + a_{31}\Delta t K_{ij}^{(3,1)} + a_{32}\Delta t K_{ij}^{(3,2)}) + a_{33}\Delta t M_{ij}^{(3)}}{\epsilon + a_{33}\Delta t}.$$

3.2.2 Stability analysis

In this subsection, we analyze linear stability of the proposed SLFD scheme coupled with the DIRK time discretization methods. Consider the linear kinetic problem

$$f_t + v f_x = \frac{1}{\epsilon}(\langle f\rangle - f), \tag{3.15}$$

with $x \in [0, 2\pi]$ and periodic boundary condition. Here $\langle f\rangle = \int_{\Omega_v} f dv$. A simple model is the one with only two discrete velocity states $\Omega_v = \{-1, 1\}$. Then (3.15) can be rewritten as the following system, with $u(x,t) = f(x, v = 1, t)$ and $v(x,t) = f(x, v = -1, t)$:

$$\begin{cases} u_t + u_x = \frac{1}{2\epsilon}(v - u), \\ v_t - v_x = \frac{1}{2\epsilon}(u - v). \end{cases} \tag{3.16}$$

We perform Von Neumann analysis to the fully discretized SLFD-DIRK scheme for solving (3.16). First, we assume the Fourier expansion of u, v:

$$u_j = \sum_k \hat{u}^{(k)}(t)e^{ij\xi}, \quad v_j = \sum_k \hat{v}^{(k)}(t)e^{ij\xi} \tag{3.17}$$

with $i = \sqrt{-1}$, $\xi = k\Delta x$ and the wave number $k = 1, 2..., \frac{N}{2}$. We first analyze SLFD-backward Euler method. Applying the first order backward Euler and a third order SLFD ($\mathcal{SL}$) method to (3.16), we obtain

$$\begin{cases} u_j^{n+1} = \mathcal{SL}[u^n(x_j - \Delta t)] + \frac{\Delta t}{2\epsilon}(v_j^{n+1} - u_j^{n+1}), \\ v_j^{n+1} = \mathcal{SL}[v^n(x_j + \Delta t)] + \frac{\Delta t}{2\epsilon}(u_j^{n+1} - v_j^{n+1}). \end{cases} \tag{3.18}$$

Here $\mathcal{SL}$ stands for a third order linear reconstruction for $u^n(x_j - \Delta t)$ and $v^n(x_j + \Delta t)$. Then, plug in the Fourier expansion of u and v (3.17), one get:

$$\begin{pmatrix} \hat{u}^{(k)}(t^{n+1}) \\ \hat{v}^{(k)}(t^{n+1}) \end{pmatrix} = \left[I - \frac{\Delta t}{2\epsilon} \begin{pmatrix} -1 & 1 \\ 1 & -1 \end{pmatrix} \right]^{-1} \begin{pmatrix} g_1(\alpha, \xi) & 0 \\ 0 & g_2(\alpha, \xi) \end{pmatrix} \begin{pmatrix} \hat{u}^{(k)}(t^n) \\ \hat{v}^{(k)}(t^n) \end{pmatrix}, \tag{3.19}$$

where $g_1(\alpha, \xi)$ and $g_2(\alpha, \xi)$ are the amplification factors of $\mathcal{SL}[u^n(x_j - \Delta t)]$ and $\mathcal{SL}[v^n(x_j + \Delta t)]$ for ξ and $\alpha = CFL$, which can be obtained from (2.9). Specifically, they are

$$\begin{aligned} g_1(\alpha, \xi) &= e^{-2i\xi}(\frac{\alpha^3}{6} + \frac{\alpha^2}{2} - \frac{\alpha}{3}) + e^{-i\xi}(-\frac{\alpha^3}{2} + \frac{\alpha^2}{2} + \alpha) + e^{i\xi}(-\frac{\alpha^3}{6} + \frac{\alpha^2}{2} - \frac{\alpha}{3}) + (\frac{\alpha^3}{2} - \alpha^2 - \frac{\alpha}{2} + 1), \\ g_2(\alpha, \xi) &= e^{2i\xi}(\frac{\alpha^3}{6} + \frac{\alpha^2}{2} - \frac{\alpha}{3}) + e^{i\xi}(-\frac{\alpha^3}{2} + \frac{\alpha^2}{2} + \alpha) + e^{-i\xi}(-\frac{\alpha^3}{6} + \frac{\alpha^2}{2} - \frac{\alpha}{3}) + (\frac{\alpha^3}{2} - \alpha^2 - \frac{\alpha}{2} + 1). \end{aligned} \tag{3.20}$$

In fact $g_2 = \bar{g}_1$. Let $b = \frac{\Delta t}{\epsilon}$, then

$$G(\alpha, b, \xi) = \left[I - \frac{b}{2} \begin{pmatrix} -1 & 1 \\ 1 & -1 \end{pmatrix} \right]^{-1} \begin{pmatrix} g_1(\alpha, \xi) & 0 \\ 0 & g_2(\alpha, \xi) \end{pmatrix} \tag{3.21}$$

is the amplification matrix, from which we assess the stability of a fully discrete scheme.

Theorem 3.1. *The proposed SLFD scheme coupled with backward Euler time discretization is unconditionally stable.*

Proof. We only prove the case when $CFL \leq 1$, the case of larger CFL can be generalized in a straightforward manner with an extra shifting operator of unit norm. We first numerically show that $|g_1(\alpha, \xi)| = |g_2(\alpha, \xi)| \leq 1$ for $CFL \in [0, 1]$ and $\xi \in [0, 2\pi]$ in Figure 3.2. We then investigate the norm of symmetric matrix

$$A = \left[I - \frac{b}{2} \begin{pmatrix} -1 & 1 \\ 1 & -1 \end{pmatrix} \right]^{-1} = \frac{1}{2(1+b)} \begin{pmatrix} 2+b & b \\ b & 2+b \end{pmatrix}.$$

Its eigenvalues are $\frac{1}{1+b}$ and 1 with $b > 0$. Thus $\|A\| \leq 1$, here $\|\cdot\|$ represents the spectral norm of a matrix, hence,

$$\|G\| \leq \|A\| \max(|g_1|, |g_2|) \leq 1.$$

□

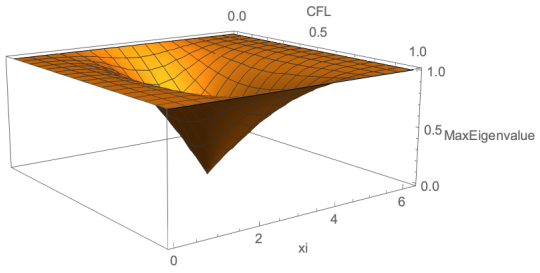

Figure 3.2: Plot of $|g_1(\alpha,\xi)|$ versus α and ξ .

For a 2-stage DIRK2 method, e.g. see the Butcher table of (7.6), we repeat the similar procedure as the backward Euler method (3.18)-(3.19) for the first time stage $t^{(1)} = t^n + c_1\Delta t$. For the second/final RK stage t^{n+1}, we have the formulation

$$\begin{cases} u_j^{n+1} = \mathcal{SL}[u^n(x_j - c_2\Delta t)] + \frac{a_{21}\Delta t}{2\epsilon}\mathcal{SL}\left[(v^{(1)} - u^{(1)})(x_j - (c_2 - c_1)\Delta t)\right] + \frac{a_{22}\Delta t}{2\epsilon}(v_j^{n+1} - u_j^{n+1}), \\ v_j^{n+1} = \mathcal{SL}[v^n(x_j + c_2\Delta t)] + \frac{a_{21}\Delta t}{2\epsilon}\mathcal{SL}\left[(u^{(1)} - v^{(1)})(x_j + (c_2 - c_1)\Delta t)\right] + \frac{a_{22}\Delta t}{2\epsilon}(u_j^{n+1} - v_j^{n+1}). \end{cases} \tag{3.22}$$

Apply the Fourier assumption to the above equations, we get

$$\begin{pmatrix} \hat{u}^{(k)}(t^{(1)}) \\ \hat{v}^{(k)}(t^{(1)}) \end{pmatrix} = A_1^{-1}B_1 \begin{pmatrix} \hat{u}^{(k)}(t^n) \\ \hat{v}^{(k)}(t^n) \end{pmatrix}, \tag{3.23}$$

$$\begin{pmatrix} \hat{u}^{(k)}(t^{n+1}) \\ \hat{v}^{(k)}(t^{n+1}) \end{pmatrix} = A_2^{-1}[B_2 + C_{21}A_1^{-1}B_1] \begin{pmatrix} \hat{u}^{(k)}(t^n) \\ \hat{v}^{(k)}(t^n) \end{pmatrix},$$

where we define,

$$A_l = \left[I - \frac{a_{ll}b}{2}\begin{pmatrix} -1 & 1 \\ 1 & -1 \end{pmatrix}\right]^{-1}, \; B_l = \begin{pmatrix} g_1(c_l\alpha,\xi) & 0 \\ 0 & g_2(c_l\alpha,\xi) \end{pmatrix}, \tag{3.24}$$

$$C_{ml} = \begin{pmatrix} -\frac{a_{ml}b}{2}g_1[(c_m - c_l)\alpha,\xi] & \frac{a_{ml}b}{2}g_1[(c_m - c_l)\alpha,\xi] \\ \frac{a_{ml}b}{2}g_2[(c_m - c_l)\alpha,\xi] & -\frac{a_{ml}b}{2}g_2[(c_m - c_l)\alpha,\xi] \end{pmatrix}. \tag{3.25}$$

for $l = 1, ..., s$ and $m > l \geq 1$.

Then we have the amplification matrix for the SLFD-DIRK2 method

$$G(\alpha, b, \xi) = A_2^{-1}\left[B_2 + C_{21}A_1^{-1}B_1\right]. \tag{3.26}$$

Figure 3.3 shows the spectral radius of $G(\xi)$ with $\xi \in [0, 2\pi]$ for the DIRK2 method (see Table 7.6) in the limit of $b \to \infty$ with $CFL \in [0, 1]$ (left plot) and with $CFL = 1$ (right plot). From this figure, we observe that $\rho(G) \leq 1$ for all $\xi \in [0, 2\pi]$. We also compute $\rho(G)$ by sampling $CFL \in [0, 1]$ and $b \in (0, \infty]$ and found that it is uniformly bounded by 1 for all $\xi \in [0, 2\pi]$.

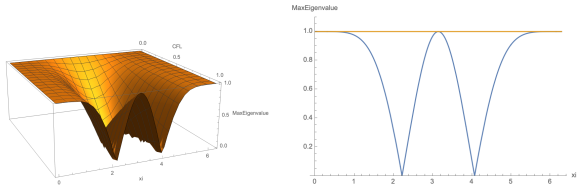

Figure 3.3: The spectral radius of amplification matrix for DIRK2 Table (7.6) as $\frac{\Delta t}{\epsilon} \to \infty$. Left: the spectral radius vs. CFL and ξ, right: the spectral radius vs. ξ when $CFL = 1$.

Similarly, we apply the proposed SLFD scheme with 3-stage and 4-stage DIRK3 methods. Their corresponding amplification matrices for Fourier modes are

$$\begin{pmatrix} \hat{u}^{(k)}(t^{n+1}) \\ \hat{v}^{(k)}(t^{n+1}) \end{pmatrix} = A_3^{-1}\left[B_3 + \sum_{l=1}^{2} C_{3l}A_l^{-1}E_l\right]\begin{pmatrix} \hat{u}^{(k)}(t^{n}) \\ \hat{v}^{(k)}(t^{n}) \end{pmatrix}, \tag{3.27}$$

$$\begin{pmatrix} \hat{u}^{(k)}(t^{n+1}) \\ \hat{v}^{(k)}(t^{n+1}) \end{pmatrix} = A_4^{-1}\left[B_4 + \sum_{l=1}^{3} C_{4l}A_l^{-1}E_l\right]\begin{pmatrix} \hat{u}^{(k)}(t^{n}) \\ \hat{v}^{(k)}(t^{n}) \end{pmatrix}. \tag{3.28}$$

where $E_l = B_l + \sum_{n=1}^{l-1} C_{ln}A_n^{-1}E_n$, and A_l, B_l, C_{ml} are defined as in (3.24)-(3.25). We investigate the stability of the 4-stage DIRK3 with the Butcher Table 7.8 by plotting the spectral radius of the associated amplification matrix in the limit of $b \to \infty$ with $CFL \in [0, 1]$ (left plot) and $CFL = 1$ (right plot) in Figure 3.4. Further more, we repeat the same plot in Figure 3.5 but for one 3-stage DIRK3 table and eight 4-stage DIRK3 tables. The Butcher tables used are listed as Table (7.7) and (7.9)-(7.16) in the Appendix. We observe that instability occurs for DIRK methods with Butcher Table (7.10), (7.11), (7.13), other tables are observed to be stable in the asymptotic limit.

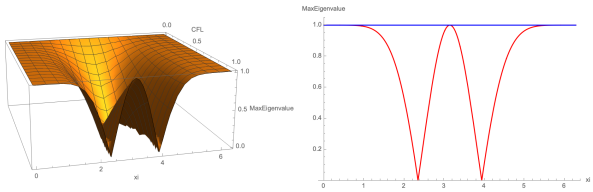

Figure 3.4: The spectral radius of amplification matrix for 4-stage DIRK3 Table (7.8) as $\frac{\Delta t}{\epsilon} \to \infty$. Left: the spectral radius vs. CFL and ξ, right: the spectral radius vs. ξ when $CFL = 1$.

4 Numerical results

In this section, the proposed SLFD-WENO scheme are tested on linear advection problems and the nonlinear VP system and BGK model.

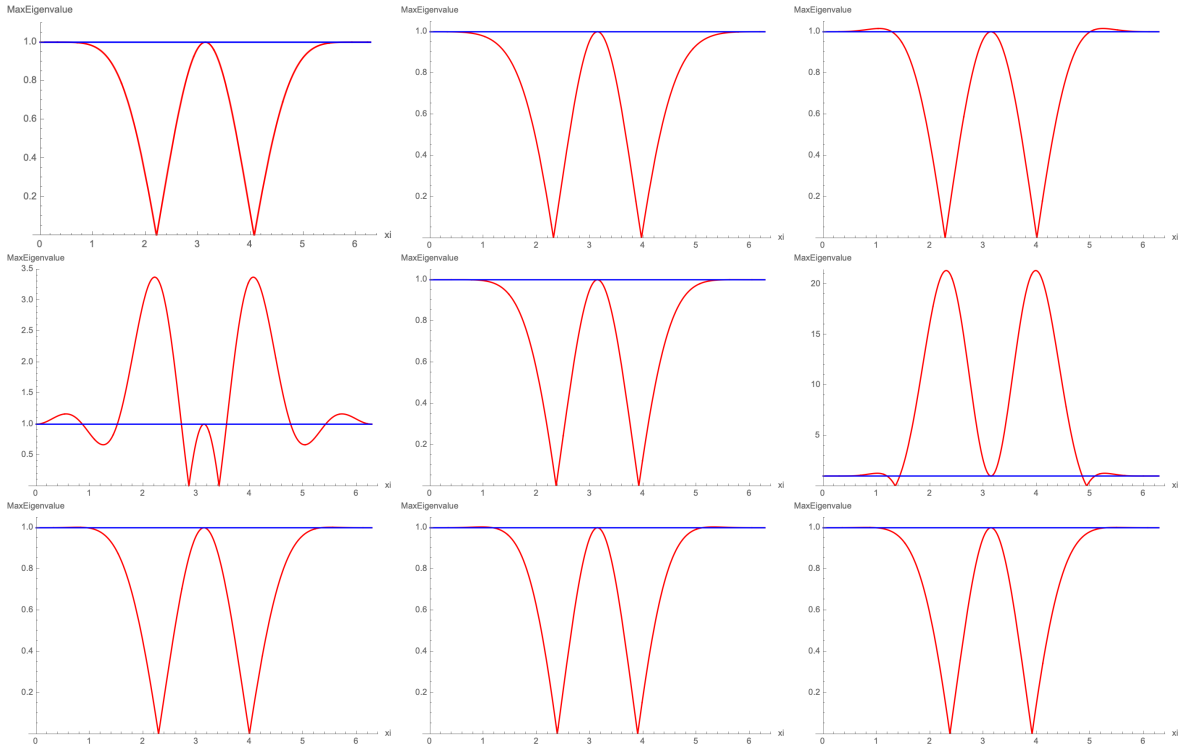

Figure 3.5: The spectral radius of amplification matrix for 4-stage DIRK3 with Butcher tables specified in Table 7.7, and Table 7.9 - Table 7.16, respectively, as $\frac{\Delta t}{\epsilon} \to \infty$ and $CFL = 1$.

4.1 2D linear advection problems

We first test our scheme by performing a second order Strang splitting for 2D linear advection problems. Each of the 1D equation is evolved by the proposed 5th order SLFD-WENO method.

Example 4.1. (2D linear advection equation) We consider the 2D linear advection equation:

$$u_t + u_x + u_y = 0, \;\; x \in [-\pi, \pi], \;\; y \in [-\pi, \pi], \tag{4.1}$$

with periodic boundary conditions and the initial condition

$$u(x, y, t = 0) = sin(x + y). \tag{4.2}$$

The errors and numerical orders of accuracy of the newly developed SLFD methods are shown in Table 4.1. Since there is no splitting error in time, the dominant error is the spatial error. In our 2D simulations, we set $CFL = \frac{\Delta t}{\Delta x} + \frac{\Delta t}{\Delta y} = 2.2$, final time $T = 3$. We observe the expected fifth order of convergence of the SLFD scheme from Table 4.1 .

Table 4.1: L^1 error and order of convergence of the SLFD WENO5 scheme for Example 4.1.

Mesh	L^1 *error*	*order*
40×40	5.49e-04	
80×80	1.63e-05	5.07
120×120	2.13e-06	5.01
160×160	5.08e-07	4.99

Example 4.2. (Rigid body rotation) We consider

$$u_t - yu_x + xu_y = 0, \;\; x \in [-\pi, \pi], \;\; y \in [-\pi, \pi], \tag{4.3}$$

with a non-symmetric initial condition.

$$u(x, y, t = 0) = e^{(-x^2-5y^2)}. \tag{4.4}$$

The L^1 error and the corresponding spatial order of convergence of SLFD-WENO scheme with $CFL = 5$ (left column) and $\Delta t = \Delta x^{2.5}$ (right column) at $T = 2\pi$ are presented in Table 4.2. Here we define $\Delta t = \frac{CFL}{\frac{vmax_x}{\Delta x} + \frac{vmax_y}{\Delta y}}$, with $vmax_x$ and $vmax_y$ are maximum transport speeds in x and y directions, respectively. Expected second order temporal convergence and fifth order spatial convergence are observed when the temporal and spatial error dominates correspondingly. Figure 4.6 presents the error vs. CFL plot, which verifies the second order Strang splitting temporal error. It is also observed that the scheme is stable under very large time stepping sizes. We then test the scheme on a set of initial condition, including a slotted disk, a cone as well as a smooth hump [15]. It is plotted in Figure 4.7. The numerical solution of the SLFD-WENO5 scheme after six full revolution is plotted in Figure 4.8 by mesh and in Figure 4.9 by slides benchmarked with the exact solution. With WENO reconstructions, non-oscillatory capturing of discontinuities is observed.

Table 4.2: L^1 error and order of accuracy for Example 4.2 with initial condition (4.4).

	CFL=5		$dt = dx^{2.5}$	
Mesh	L^1 *error*	*order*	L^1 *error*	*order*
40×40	4.58e-02		6.77e-02	
80×80	3.75e-03	3.61	5.11e-03	3.71
120×120	8.96e-04	3.53	8.51e-04	4.42
160×160	4.39e-04	2.48	2.25e-04	4.63

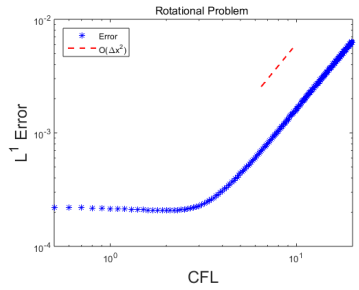

Figure 4.6: Error vs. CFL plot for non-symmetric initial condition (4.4).

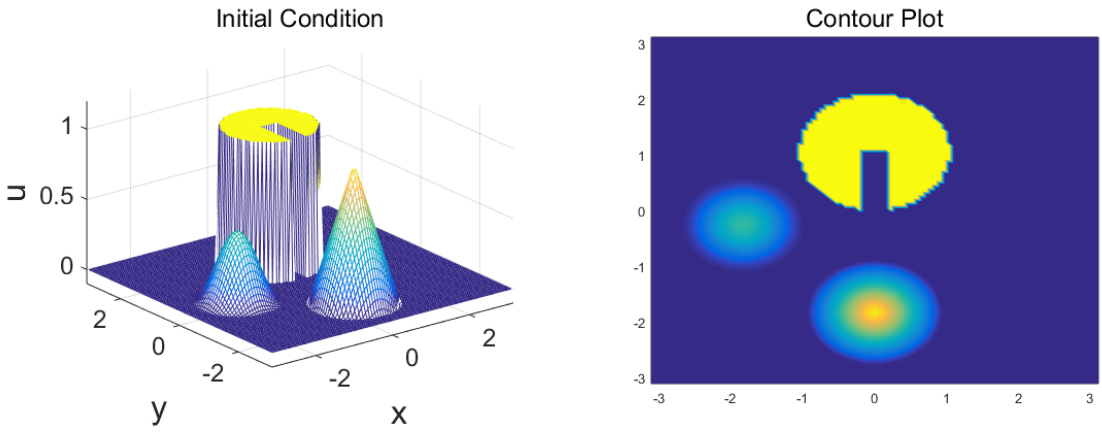

Figure 4.7: Plots of initial data. Numerical mesh is 100×100.

4.2 The VP System

In this subsection, we apply the SLFD-WENO scheme to the nonlinear Vlasov model via a few classical test cases such as the Landau damping and two-stream instability.

Example 4.3. (Landau damping) We first consider the weak Landau damping for the VP system with the initial condition

$$f(x, v, t = 0) = \frac{1}{\sqrt{2\pi}}(1 + \alpha cos(kx))exp(\frac{-v^2}{2}) \tag{4.5}$$

where $\alpha = 0.01$ and $k = 0.5$. Our numerical simulations parameters are $v_{max} = 5$, $N_x = N_v = 128$, $CFL = 2.5$ and final integration time is $T = 60$. The time evolution of the L^2 norms of the electric field are plotted, benchmarked with the theoretical value $\gamma = 0.1533$ (red line) in the first plot of Figure 4.10. The time evolution of the L^1, L^2 norms of solution, energy and entropy in the discrete sense are presented in Figure 4.10. We remark that in the weak Landau damping case, the

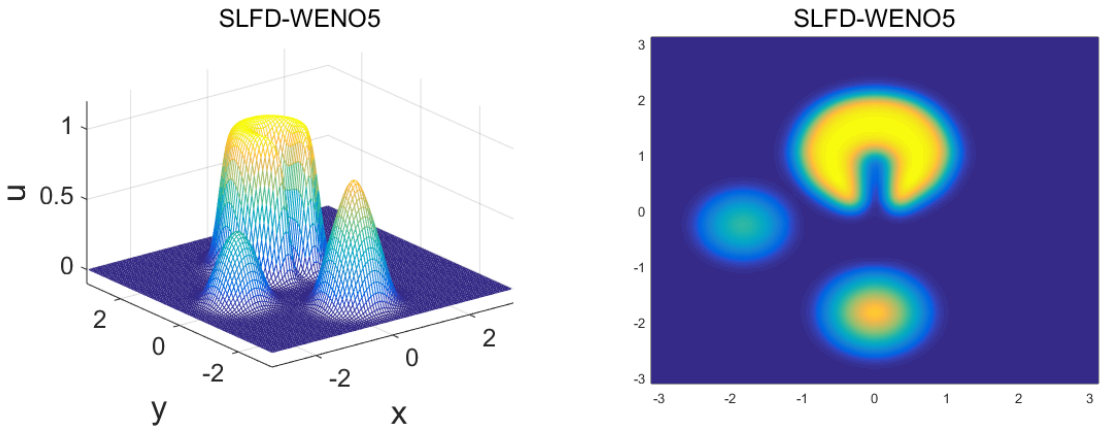

Figure 4.8: Numerical solutions for Example 4.2. $T = 12\pi$. The numerical mesh is 100×100 and $CFL = 2$.

relevant physical norms are preserved well. Next we consider the strong Landau damping using the initial condition in (4.5) with $\alpha = 0.5$ and $k = 0.5$. The numerical simulation parameters for both schemes are $v_{max} = 5$, $N_x = N_v = 128$ and $CFL = 2.5$, where v_{max} is the maximum velocity on the phase space mesh. The time evolution of the L^2 norm of the electric field, is benchmarked with the linear decay rate $\gamma_1 = -0.2812$ and $\gamma_2 = 0.0770$ [3] as plotted in the first plot of Figure 4.11. The time evolution of the L^1, L^2 norms of the solution, energy and entropy in the discrete sense are presented in order in Figure 4.11. The L^1 norm is not exactly preserved, due to the lack of positivity preserving property of the scheme. A polynomial rescaling limiter [18] could be applied to preserve the positivity, hence the L^1 norm of the solution.

Example 4.4. (Two stream instability [8]) Consider two stream instability with an unstable initial condition

$$f(x, v, t = 0) = \frac{2e^{\frac{-v^2}{2}}}{7\sqrt{2\pi}} \left(1 + 5v^2\right) \left(1 + \alpha \frac{cos(2kx) + cos(3kx)}{1.2} + cos(kx)\right) \tag{4.6}$$

where $\alpha = 0.01$, $k = 0.5$. The length of the domain in the x direction is $L = \frac{2\pi}{k}$ and the background ion distribution function is fixed, uniform and chosen so that the total net charge density for the system is zero. Our simulation parameters are $v_{max} = 5$, $N_x = N_v = 128$, $CFL = 2.2$. The first row of Figure 4.12 shows the contour plot of numerical solution at $T = 60$, as well as the L^2 norm of the electric field. The time evolution of the L^1, L^2 norms of solution, energy and entropy in the discrete sense are also presented in Figure 4.12.

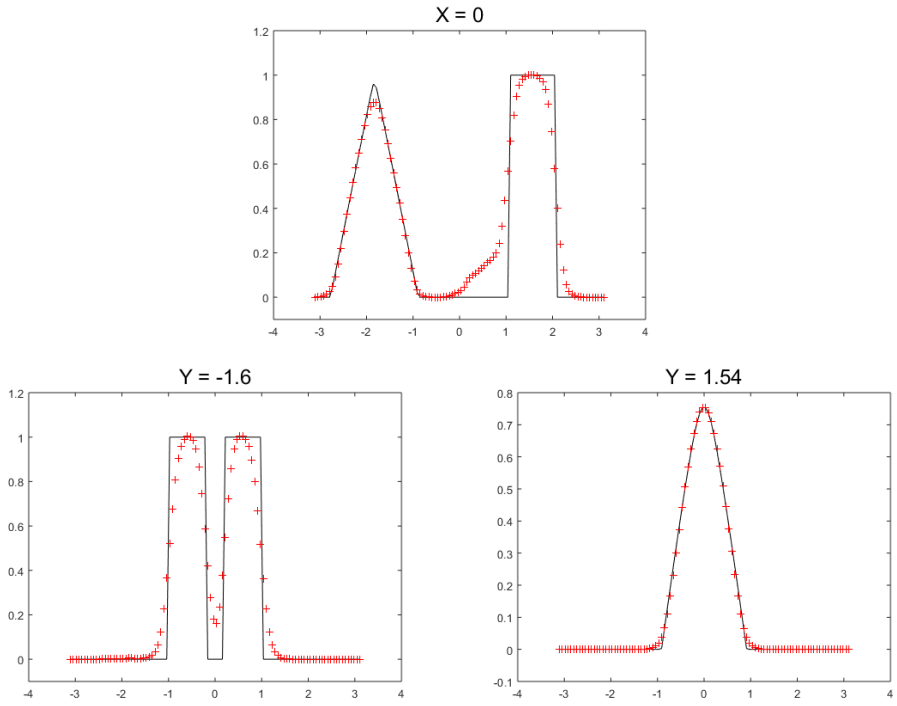

Figure 4.9: Plots of slides of numerical solution in Figure 4.8 at $X = 0$, $Y = -1.6$ and $Y = 1.54$.

4.3 Application to the BGK model

In this subsection, we apply the SLFD-WENO coupled with DIRK schemes along characteristics on the stiff relaxation models, which include the linear two-velocity model and the nonlinear BGK model. While the stability of the algorithm is analyzed in section 3.2.2 and the asymptotic accuracy property is analyzed in [7], we numerically investigate the stability and accuracy properties of various SLFD-DIRK schemes.

Example 4.5. (Two-velocity problem) We consider solving the linear two-velocity model (3.16) with the proposed SLFD-WENO scheme coupled with backward Euler method, two-stage DIRK2 (Table 7.6), 3-stage DIRK3 (Table 7.7) and 4-stage DIRK3 (Table 7.8) methods. Initial condition is given by

$$u(x,0) = exp(sin(2\pi x)),\ v(x,0) = exp(sin(2\pi x)),\ x \in [0,1]. \tag{4.7}$$

To avoid the initial layer, numerical solutions starts from $t = 1$ and the final computational time is $t = 2$. The time stepping size $\Delta t = CFL \cdot \Delta x$. We provide a CFL-error plot in Figure 4.13. When $CFL \leq 1$, our numerical results are consistent with linear stability analysis. DIRK3 schemes with

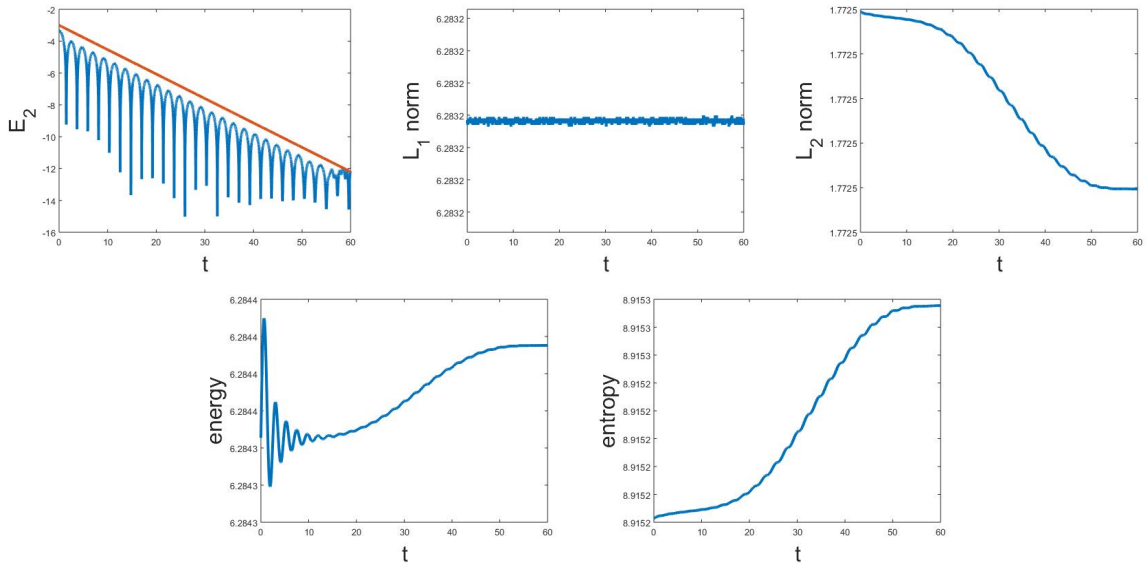

Figure 4.10: Weak Landau damping: time evolution of electric field in L^2 norms, L^1 norms and L^2 norms of the solution as well as the discrete kinetic energy and entropy.

Butcher tables such as in Table 7.8 and Table 7.9 are stable, while instability showed up for the DIRK3 scheme Table 7.11 for which the the spectral radius of amplification matrix is greater than 1. When CFL is greater than 1, for which our linear stability analysis does not cover, instability shows up for many DIRK3 schemes when the Knudsen number $\epsilon = 10^{-6}$.

Example 4.6. (BGK model [11]) We consider (3.5) with the initial Maxwellian distribution from macroscopic fields

$$f(x, v, 0) = \frac{\rho}{\sqrt{2\pi RT}} \cdot exp(-\frac{(v - u_0(x))^2}{2RT}), \tag{4.8}$$

with $\rho = 1$, and $T = 1$, $R = 1$ and

$$u = 0.1exp(-(10x - 1)^2) - 2exp(-(10x + 3)^2),\ x \in [-1, 1],\ v \in [-10, 10]. \tag{4.9}$$

Periodic boundary condition is considered. Uniformly spaced $N_v = 40$ points are used for velocity domain $[-10, 10]$. We set $\Delta t = CFL\Delta x/v_{max}$ with $CFL = 4$. In Table 4.3, we show the L^1 errors and spatial orders of convergence for the SLFD-WENO5 scheme with several Knudsen numbers ϵ at $t = 0.04$. The expected third order accuracy are observed when ϵ is of order 1. For the 3-stage DIRK3 method (7.7), order reduction with only second order convergence is observed when $\epsilon = 1.e - 6$. Full third order convergence is observed for other 4-stage DIRK3 methods. We refer readers to [7] for the discussion on asymptotic accuracy of DIRK methods when solving stiff

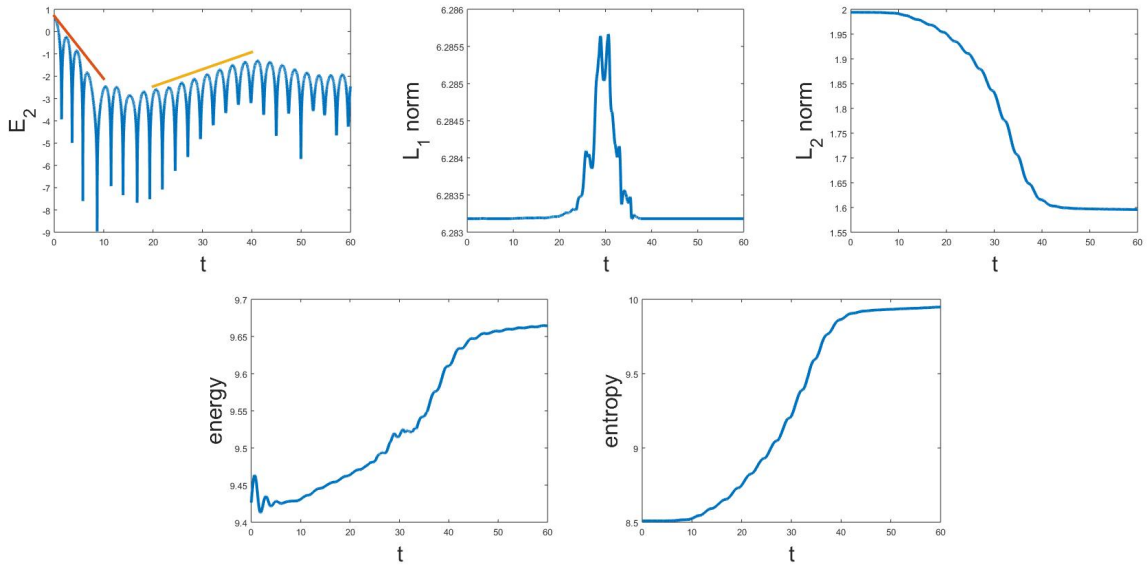

Figure 4.11: Strong Landau damping: time evolution of electric field in L^2 norms, L^1 and L^2 norms of the solution as well as the discrete kinetic energy and entropy.

relaxation models along characteristics. In Figure 4.14, the temporal error of the proposed SLFD-WENO5 methods coupled with Backward Euler, DIRK2 and DIRK3 method when $\epsilon = 10^{-2}$ and $\epsilon = 10^{-6}$, are presented together with the reference slopes. It is observed that CFL can be chosen as large as 10 thanks to the SL scheme, and that third-order convergence is observed for the 4-stage DIRK3 method for both the kinetic and fluid regimes. Classical 3-stage DIRK3 method can only achieve second order accuracy when in fluid regimes.Table 4.4 shows that our scheme preserves the conservation of the macroscopic fields well when the mesh for the velocity is sufficiently refined.

Example 4.7. (Inconsistent initial data [14]) Consider the inconsistent initial data,

$$f(x,v,0) = 0.5\frac{\rho}{\sqrt{2\pi RT}} \cdot exp(-\frac{(v-u_0(x))^2}{2RT}) + 0.3\frac{\rho}{\sqrt{2\pi RT}} \cdot exp(-\frac{(v+0.5u_0(x))^2}{2RT}) \tag{4.10}$$

where $x \in [-1,1]$, and $u_0 = 1, \rho_0 = 1.0 + 0.2sin(\pi x), T_0 = \frac{1}{\rho_0}$. f is a linear combination of two Gaussian distribution centered around different macroscopic velocities. We show in Table 4.5 the L^1 error and order of convergence. As expected, third order accuracy is observed in the kinetic regime and only first order accuracy is observed in the fluid regime.

Example 4.8. (Riemann Problem [19]) We test the capability of our schemes in capturing shocks and contact discontinuities by considering a Riemann problem in the fluid regime. The initial

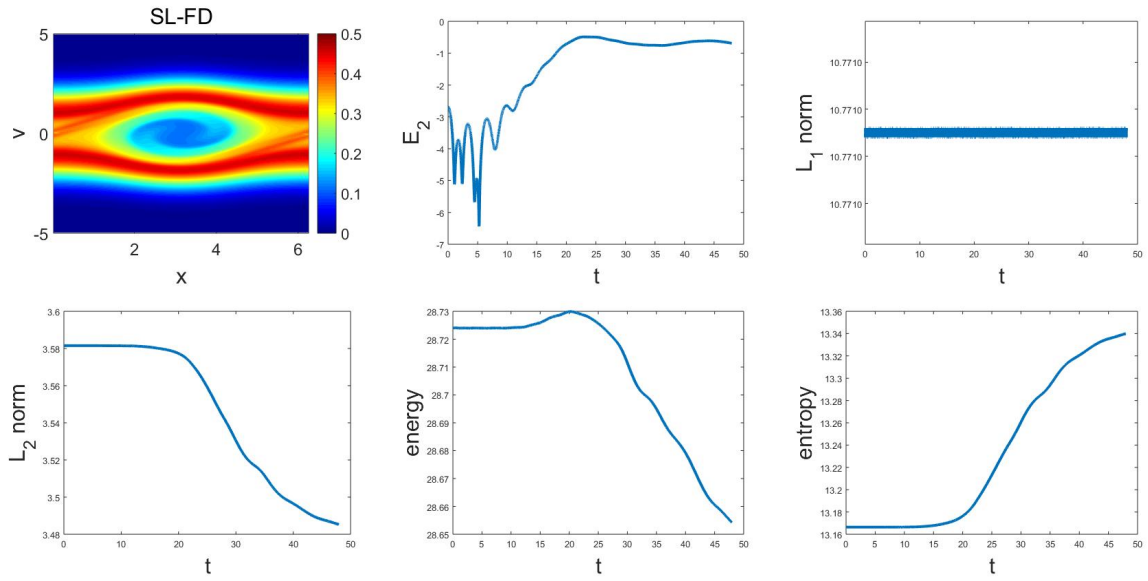

Figure 4.12: Two stream instability: contour plot of the solution (top left), time evolution of electric field in L^2 norm (top right), solution's L^1 and L^2 norms as well as the discrete kinetic energy and entropy.

Table 4.3: Example 4.6. SLFD-WENO coupled with DIRK schemes with $CFL = 4$. $T = 0.04$.

N_x	$\epsilon = 1$		$\epsilon = 10^{-2}$		$\epsilon = 10^{-6}$	
DIRK3-Table 7.7	L^1 error	Order	L^1 error	Order	L^1 error	Order
10	0.03		0.04		0.04	
30	0.0017	2.62	0.0015	2.93	0.0020	2.68
90	3.2545e-05	3.62	3.54e-05	3.39	1.75e-04	2.20
270	1.5491e-07	4.93	1.27e-06	3.03	1.66e-05	2.15
DIRK3-T1	L^1 error	Order	L^1 error	Order	L^1 error	Order
10	0.03		0.04		0.04	
30	0.0017	2.63	0.0015	2.96	0.0017	2.89
90	3.19e-05	3.59	2.48e-05	3.75	3.01e-05	3.69
270	1.43e-07	4.95	2.02e-07	4.38	7.99e-07	3.30
DIRK3-T2	L^1 error	Order	L^1 error	Order	L^1 error	Order
10	0.03		0.04		0.04	
30	0.0017	2.63	0.0015	2.94	0.0017	2.86
90	3.25e-05	3.59	2.47e-05	3.75	2.81e-05	3.76
270	1.41e-07	4.95	2.64e-07	4.13	2.61e-07	4.26

distribution function is

$$f(x,v,0) = \begin{cases} \rho_L(2\pi RT_L)^{-1/2} \cdot exp(-\frac{(u_L-v)^2}{2RT_L}), 0 \le x \le 0.5 \\ \rho_R(2\pi RT_R)^{-1/2} \cdot exp(-\frac{(u_R-v)^2}{2RT_R}), 0.5 < x \le 1 \end{cases} \tag{4.11}$$

where the moments are being taken as $(\rho_L, u_L, T_L) = (2.25, 0, 1.125)$ and $(\rho_R, u_R, T_R) = (3/7, 0, 1/6)$. Free-flow boundary conditions are assumed. For the time discretization, we use the 4-stage DIRK3

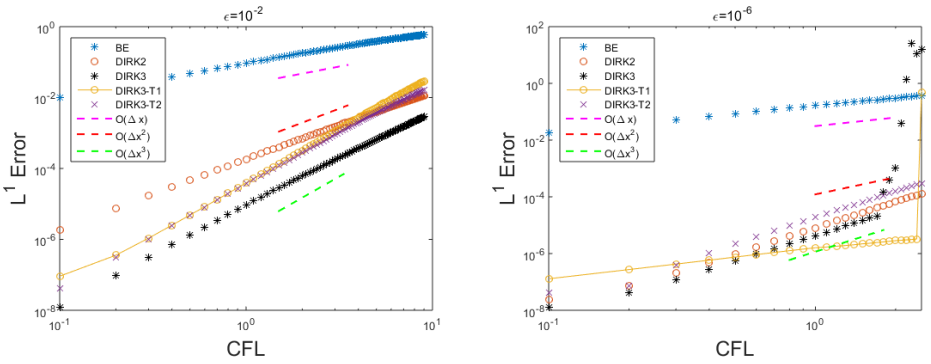

Figure 4.13: Example 4.5 L^1 error vs. CFL on a fixed mesh of $N_x = 200$. $CFL = 0.001$ is used as the reference solution to compute the L^1 error. Butcher tables of the specific third order DIRK schemes are provided in the Appendix.

Table 4.4: Conservation of macroscopic fields. $CFL = 4$, $N_x = 80$, $t = 0.1$.

N_v Mesh	$\epsilon = 10^{-2}$			$\epsilon = 10^{-6}$		
DIRK2	ρ	ρu	E	ρ	ρu	E
20	-1.03e-07	-6.39e-08	1.87e-06	-4.72e-07	-3.46e-07	8.52e-06
100	-9.44e-16	7.40e-16	-3.05e-16	2.51e-12	-3.40e-14	1.27e-12
DIRK3-T1	ρ	ρu	E	ρ	ρu	E
20	-1.18e-07	-7.36e-08	2.15e-06	-1.09e-06	-8.05e-07	1.96e-06
100	2.08e-16	2.37e-15	-9.71e-17	-1.51e-11	1.83e-13	-5.81e-12
DIRK3-T2	ρ	ρu	E	ρ	ρu	E
20	-1.06e-07	-6.64e-08	1.94e-06	-5.54e-07	-4.10e-07	1.00e-05
100	1.89e-16	2.14e-15	-1.10e-16	7.85e-12	2.31e-14	3.85e-12

Table 4.5: Example 4.7 with $CFL = 4$. SLFD-WENO coupled with DIRK schemes with $CFL = 4$. $T = 0.1$

Mesh	$\epsilon = 1$		$\epsilon = 10^{-2}$		$\epsilon = 10^{-6}$	
DIRK3-T1	L^1 error	Order	L^1 error	Order	L^1 error	Order
10	5.03e-04		0.0025		0.0128	
30	2.19e-06	4.95	1.14e-04	2.82	0.0040	1.07
90	1.59e-08	4.48	4.20e-06	3.00	0.0012	1.07
270	4.90e-10	3.17	1.46e-07	3.06	3.08e-04	1.26
DIRK3-T2	L^1 error	Order	L^1 error	Order	L^1 error	Order
10	5.03e-04		0.0013		0.0048	
30	2.19e-06	4.95	8.54e-05	2.48	0.0015	1.08
90	1.65e-08	4.45	3.69e-06	2.86	4.51e-04	1.07
270	5.35e-10	3.12	1.36e-07	3.01	1.13e-04	1.26

method with the Butcher Table 7.8. We plot macroscopic moments, i.e. the density, mean velocity and temperature for $\epsilon = 10^{-2}$ and $\epsilon = 10^{-6}$ in Figure 4.15 and Figure 4.16. The SLFD DIRK3 scheme is able to capture the fluid dynamic limit as well as solutions with sharp gradients.

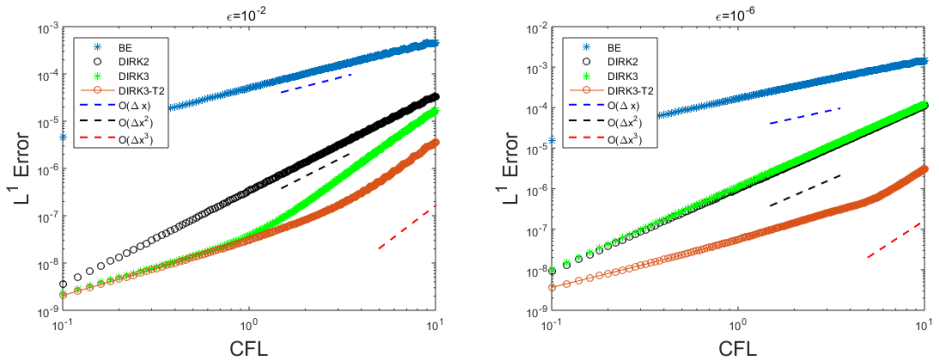

Figure 4.14: Example 4.6: L^1 error vs. CFL on fixed mesh $N_x = 270$. $CFL = 0.01$ is used as the reference solution to compute the L^1 error. Butcher tables of the specific third order DIRK schemes are provided in the Appendix.

5 Conclusion

In this paper, we developed a semi-Lagrangian finite difference scheme with WENO reconstruction process for simulating linear advection and nonlinear Vlasov and BGK systems. Linear stability analysis, for the fully discrete scheme when applied to a two-velocity relaxation model, is performed and numerically verified. Extensive numerical tests have been performed to assess the accuracy, stability and asymptotic behavior of the proposed schemes. In the future, we wish to extend the SL scheme development along with the stability analysis to the scheme with BDF time discretization for stiff relaxation models.

6 Conflict of interest statement

On behalf of all authors, the corresponding author states that there is no conflict of interest.

7 Appendix: Butcher tableaus for DIRK methods

$$\begin{array}{c|cc} \nu & \nu & 0 \\ 1 & 1-\nu & \nu \\ \hline & 1-\nu & \nu \end{array}, \qquad \nu = 1 - \frac{\sqrt{2}}{2}.$$

Table 7.6: DIRK2

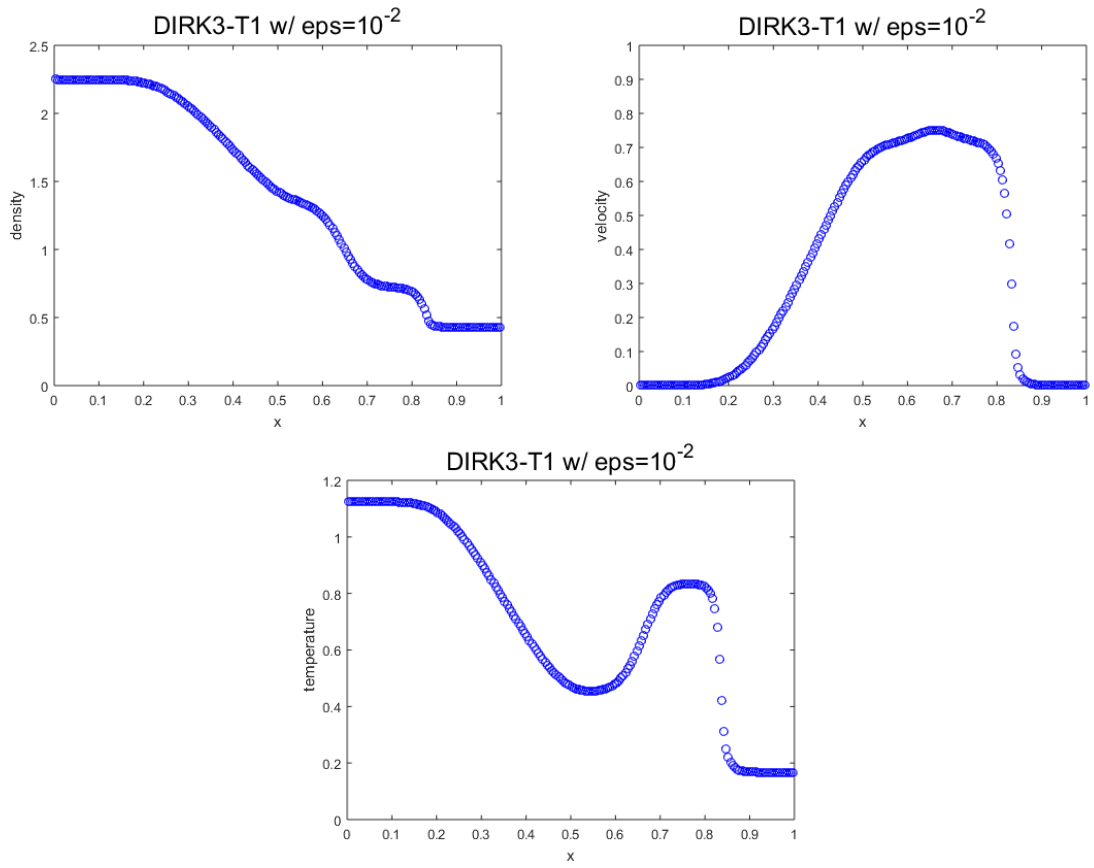

Figure 4.15: Macroscopic moments for Example 4.8 with $\epsilon = 10^{-2}$ using SLFD-WENO scheme coupled with DIRK3 Table 7.8. $T = 0.16$, $CFL = 2$, $N_x = 200$ and $N_v = 40$.

$$\begin{array}{c|cccc} \gamma & \gamma & & & \\ \frac{1+\gamma}{2} & \frac{1-\gamma}{2} & \gamma & & \\ 1 & 1-\delta-\gamma & \delta & \gamma & \\ \hline & 1-\delta-\gamma & \delta & \gamma & \end{array}, \qquad \gamma = 0.4358665215,\ \delta = -0.644363171$$

Table 7.7: 3-stage DIRK3

References

[1] S. Boscarino, S.-Y. Cho, G. Russo, and S.-B. Yun. High order conservative semi-lagrangian scheme for the bgk model of the boltzmann equation. *arXiv preprint arXiv:1905.03660*, 2019.

[2] J. Carrillo and F. Vecil. Nonoscillatory interpolation methods applied to Vlasov-based models. *SIAM Journal on Scientific Computing*, 29(3):1179–1206, 2007.

[3] C.-Z. Cheng and G. Knorr. The integration of the Vlasov equation in configuration space.

0.127224858518235	0.127224858518235			
0.331603489550386	0.204378631032151	0.127224858518235		
0.989624239986447	0	0.862399381468212	0.127224858518235	
1	0	0.746092420734223	0.126682720747542	0.127224858518235
	0	0.746092420734223	0.126682720747542	0.127224858518235

Table 7.8: 4-stage DIRK3-T1

$\frac{1}{4}$	$\frac{1}{4}$			
$\frac{11}{28}$	$\frac{1}{7}$	$\frac{1}{4}$		
$\frac{1}{3}$	$\frac{61}{144}$	$-\frac{49}{144}$	$\frac{1}{4}$	
1	0	0	$\frac{3}{4}$	$\frac{1}{4}$
	0	0	$\frac{3}{4}$	$\frac{1}{4}$

Table 7.9: 4-stage DIRK3-T2

1.482285978970554	1.482285978970554			
0.840649305846235	-0.6416366731243188	1.482285978970554		
0.369773737448817	0.849139645385794	-1.961651886907531	1.482285978970554	
1	-0.1539440520308502	-1.343634476018696	1.015292549078992	1.482285978970554
	-0.1539440520308502	-1.343634476018696	1.015292549078992	1.482285978970554

Table 7.10: 4-stage DIRK3-T3

2.27150570419991	2.27150570419991			
3.056226528893545	0.7847208246936352	2.27150570419991		
1.562647551086182	-0.1820073706066531	-0.5268507825070748	2.27150570419991	
1	-0.3087181277990522	-0.2907425312065166	-1.253530107607374	2.27150570419991
	-0.3087181277990522	-0.2907425312065166	-1.253530107607374	2.27150570419991

Table 7.11: 4-stage DIRK3-T4

0.1376586577601238	0.1376586577601238			
0.5601286538192144	0.4224699960590905	0.1376586577601238		
0.6273053597634042	0.3693098698936377	0.1203368321096427	0.1376586577601238	
1	0.330756291090243	0.2479472066914047	0.2836378444582285	0.1376586577601238
	0.330756291090243	0.2479472066914047	0.2836378444582285	0.1376586577601238

Table 7.12: 4-stage DIRK3-T5

4.025563222205342	4.025563222205342			
2.891263084714272	-1.13430013749107	4.025563222205342		
1.871613091897857	0.8450375691764959	-2.998987699483981	4.025563222205342	
1	-1.33950660036402	4.925563641076701	-6.611620262918024	4.025563222205342
	-1.33950660036402	4.925563641076701	-6.611620262918024	4.025563222205342

Table 7.13: 4-stage DIRK3-T6

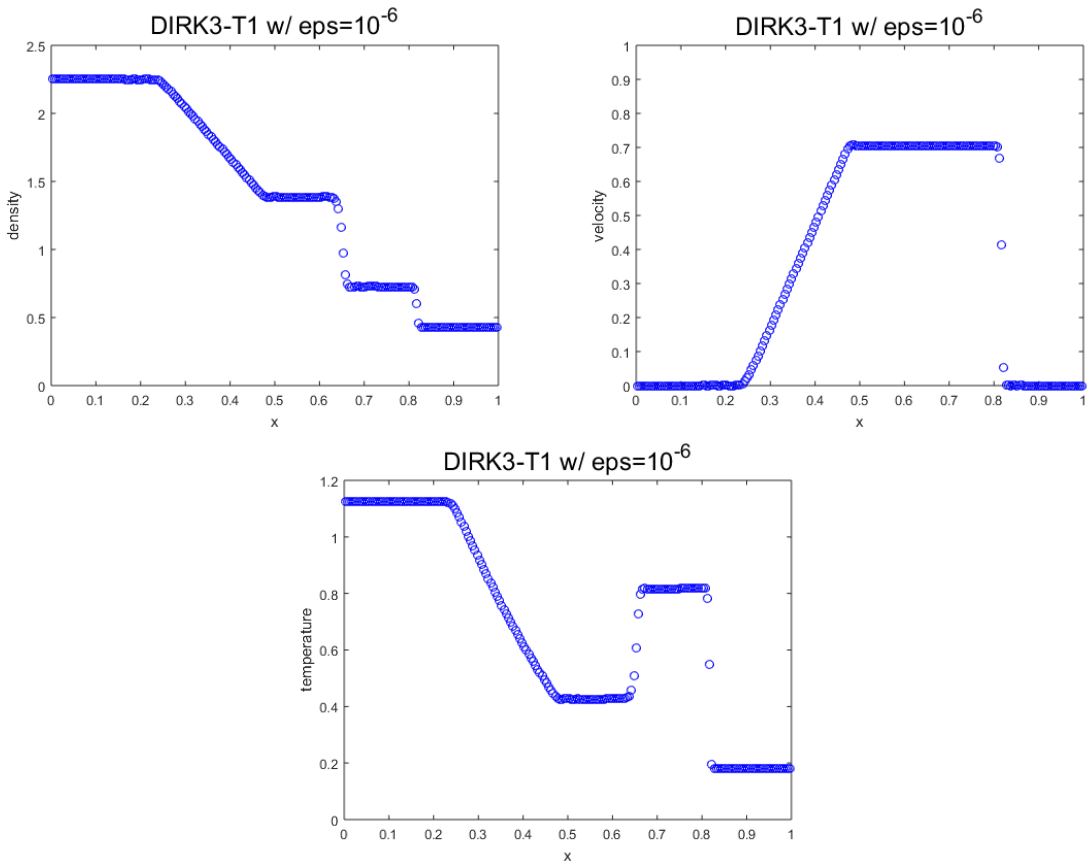

Figure 4.16: Macroscopic moments for Example (4.8) with $\epsilon = 10^{-6}$ using SLFD-WENO scheme coupled with DIRK3 Table 7.8. $T = 0.16$, $CFL = 2$, $N_x = 200$ and $N_v = 40$.

Journal of Computational Physics, 22(3):330–351, 1976.

[4] N. Crouseilles, M. Mehrenberger, and E. Sonnendrücker. Conservative semi-Lagrangian schemes for Vlasov equations. *Journal of Computational Physics*, 229(6):1927–1953, 2010.

[5] N. Crouseilles, M. Mehrenberger, and E. Sonnendrücker. Conservative semi-Lagrangian schemes for Vlasov equations. *Journal of Computational Physics*, 229(6):1927–1953, 2010.

[6] M. Ding, X. Cai, W. Guo, and J.-M. Qiu. A semi-Lagrangian discontinuous Galerkin (DG)–local DG method for solving convection-diffusion equations. *Journal of Computational Physics*, 409:109295, 2020.

[7] M. Ding, J.-M. Qiu, and R. Shu. Accuracy and stability analysis of the Semi-Lagrangian method for stiff hyperbolic relaxation systems and kinetic BGK model. *In preparation*.

$\frac{1}{2}$	$\frac{1}{2}$			
$\frac{1}{4}$	$-\frac{1}{4}$	$\frac{1}{2}$		
$\frac{3}{2}$	-1	2	$\frac{1}{2}$	
1	$-\frac{1}{12}$	$\frac{2}{3}$	$-\frac{1}{12}$	$\frac{1}{2}$
	$-\frac{1}{12}$	$\frac{2}{3}$	$-\frac{1}{12}$	$\frac{1}{2}$

Table 7.14: 4-stage DIRK3-T7

0.153198102889014	0.153198102889014			
0.601231025797714	0.448032922908699	0.153198102889014		
0.174793845034303	0	0.021595742145288	0.153198102889014	
1	0	0.466155735240408	0.380646161870577	0.153198102889014
	0	0.466155735240408	0.380646161870577	0.153198102889014

Table 7.15: 4-stage DIRK3-T8

[8] F. Filbet and E. Sonnendrücker. Comparison of Eulerian Vlasov solvers. *Computer Physics Communications*, 150(3):247–266, 2003.

[9] F. Filbet, E. Sonnendrücker, and P. Bertrand. Conservative numerical schemes for the Vlasov equation. *Journal of Computational Physics*, 172(1):166–187, 2001.

[10] S. Gottlieb, D. Ketcheson, and C.-W. Shu. High order strong stability preserving time discretizations. *J. Sci. Comput.*, 38(3):251–289, 2009.

[11] M. Groppi, G. Russo, and G. Stracquadanio. High order semi-Lagrangian methods for the BGK equation. *arXiv preprint arXiv:1411.7929*, 2014.

[12] W. Guo, R. D. Nair, and J.-M. Qiu. A conservative semi-Lagrangian discontinuous Galerkin scheme on the cubed sphere. *Monthly Weather Review*, 142(1):457–475, 2014.

[13] L. M. Harris, P. H. Lauritzen, and R. Mittal. A flux-form version of the conservative semi-lagrangian multi-tracer transport scheme (cslam) on the cubed sphere grid. *Journal of Computational Physics*, 230(4):1215–1237, 2011.

0.193031472980198	0.193031472980198			
0.087206714188908	-0.105824758791290	0.193031472980198		
0.479857673328132	0	0.286826200347934	0.193031472980198	
1	0	0.204409312996206	0.602559214023597	0.193031472980198
	0	0.204409312996206	0.602559214023597	0.193031472980198

Table 7.16: 4-stage DIRK3-T9

[14] J. Hu, R. Shu, and X. Zhang. Asymptotic-preserving and positivity-preserving implicit-explicit schemes for the stiff BGK equation. *SIAM Journal on Numerical Analysis*, 56(2):942–973, 2018.

[15] R. LeVeque. High-resolution conservative algorithms for advection in incompressible flow. *SIAM Journal on Numerical Analysis*, 33(2):627–665, 1996.

[16] S.-J. Lin and R. B. Rood. Multidimensional flux-form semi-Lagrangian transport schemes. *Monthly Weather Review*, 124(9):2046–2070, 1996.

[17] X.-D. Liu, S. Osher, and T. Chan. Weighted essentially non-oscillatory schemes. *Journal of Computational Physics*, 115(1):200–212, 1994.

[18] Y. Liu, C.-W. Shu, and Z. M. On the positivity of linear weights in WENO approximations. *Acta Math Applicatae Sinica*, to appear.

[19] S. Pieraccini and G. Puppo. Implicit–explicit schemes for BGK kinetic equations. *Journal of Scientific Computing*, 32(1):1–28, 2007.

[20] J.-M. Qiu and A. Christlieb. A conservative high order semi-Lagrangian WENO method for the Vlasov equation. *Journal of Computational Physics*, 229(4):1130–1149, 2010.

[21] J.-M. Qiu and C.-W. Shu. Conservative high order semi-Lagrangian finite difference WENO methods for advection in incompressible flow. *Journal of Computational Physics*, 230(4):863–889, 2011.

[22] G. Russo and F. Filbet. Semilagrangian schemes applied to moving boundary problems for the BGK model of rarefied gas dynamics. *Kinetic and Related Models*, 2(1):231–250, 2009.

[23] G. Russo, P. Santagati, and S.-B. Yun. Convergence of a semi-Lagrangian scheme for the BGK model of the Boltzmann equation. *SIAM Journal on Numerical Analysis*, 50(3):1111–1135, 2012.

[24] G. Russo and S.-B. Yun. Convergence of a semi-Lagrangian scheme for the ellipsoidal BGK model of the Boltzmann equation. *SIAM Journal on Numerical Analysis*, 56(6):3580–3610, 2018.

[25] C.-W. Shu. High order weighted essentially non-oscillatory schemes for convection dominated problems. *SIAM Rev.*, 51:82–126, 2009.

[26] C.-W. Shu and S. Osher. Efficient implementation of essentially non-oscillatory shock-capturing schemes. *Journal of Computational Physics*, 77(2):439–471, 1988.

[27] T. Umeda, M. Ashour-Abdalla, and D. Schriver. Comparison of numerical interpolation schemes for one-dimensional electrostatic Vlasov code. *J. Plasma Phys.*, 72(06):1057–1060, 2006.

[28] G. Wanner and E. Hairer. *Solving ordinary differential equations II*. Springer Berlin Heidelberg, 1996.